INTERNATIONAL JOURNAL FOR NUMERICAL METHODS IN FLUIDS, VOL. 16, 739–753 (1993)

NUMERICAL ANALYSIS OF WALL PRESSURE AND HEAT FLUX FLUCTUATIONS IN SHOCK–TURBULENT-BOUNDARY-LAYER INTERACTION

R. C. MEHTA

Aerodynamics Division, Vikram Sarabhai Space Centre, Trivandrum 695 022, India

AND

V. M. K. SASTRI

Department of Mechanical Engineering, Indian Institute of Technology, Madras 600 036, India

SUMMARY

The unsteady, compressible, Reynolds-averaged Navier–Stokes equations are solved numerically for an oblique shock-wave-induced turbulent boundary layer separation. For the freestream Mach number 6 and the freestream Reynolds number $66{\cdot}1 \times 10^6\ m^{-1}$, a time-dependent computation is performed, using MacCormack's explicit–implicit finite difference method with 82×42 grid points. A two-layer eddy viscosity turbulence model is employed in conjunction with a relaxation modification. Comparisons of the mean wall pressure and the mean heat transfer coefficient with the available experimental results are made and the evaluation of unsteady data for surface pressure and heat flux fluctuations is presented. It is found that the fluctuations in heat flux have qualitatively the same features as those of wall pressure but are different quantitatively.

KEY WORDS Numerical computation Shock-turbulent problem Spectral analysis

INTRODUCTION

With rapid advancements in computer technology and efficient numerical algorithms, computer-aided design of high-speed vehicles has started playing a decisive role in recent years. The fluid dynamics problem associated with high-speed vehicles requires in-depth aerodynamic investigations. Thus, a strong link between computational fluid dynamics scientists and the practical designer has to be well established.

Large shear stress gradients normal to the surface are set up in the inner region due to shock–turbulent-boundary-layer interaction. They drag low-energy air downstream into the region of high pressure. At a sufficiently large pressure rise in the shock wave interaction region, the boundary layer is separated, forming a bubble of reversed flow adjacent to the wall. This low-energy constituent of the boundary layer continues to be trapped in the separation bubble. Therefore, the information regarding the movement of separation and reattachment points and the turbulent convection of recirculating flow is of major concern to the aerodynamic engineer. The unsteady feature of a turbulent separating flow shows an intermittent character of separation. Thus, the aerodynamic 'noise' level and the corresponding frequencies for unsteady

0271–2091/93/080739–15$12.50

Received February 1992
Revised November 1992

pressure oscillations near the interaction region are also required in order to maintain the structural integrity of the system.

Kistler[1] has shown that the surface pressure signal near separation in forward spacing at freestream Mach numbers of 3·01 and 4·54 can be modelled as a step function, with the shock wave moving over the same range. Measurements of wall pressure fluctuations by Kistler near separation revealed the intermittent nature of the wall pressure signal, which was attributed to the unsteady separation shock wave. Dolling and Murphy[2] have observed an inherent character of oscillation of the separation shock wave in the interaction region of a compression corner at a freestream Mach number of 4. There are other observations about the unsteadiness in a variety of high-speed flows, such as sharp fins at the angle of attack[3] and in shock-impinging regions.[4] Coe *et al.*[5] have studied a large amount of experimental data to determine the characteristics of surface pressure fluctuations underlining supersonic attached and separated turbulent boundary layers, and regions of shock waves over a Mach number range of 1·6–3·5. Various experimental wall pressure fluctuation results were studied and summarized in a recent article of Dolling and Dussauge.[6] However, these experimental efforts were limited mainly to pressure fluctuations.

Hayashi *et al.*[7] have recently measured the fluctuating heat flux in the interaction region of oblique incident shock wave and turbulent boundary layer interaction. They measured strong pressure and heat flux fluctuations near the separation and reattachment points.

The main purpose of the present numerical analysis is to compute the mean and the fluctuating flow along the flat plate, the range of sound pressure levels (dB), and the fluctuations of heat flux and the corresponding frequencies.

GOVERNING EQUATIONS

A planar oblique shock strikes on a flat plate at a freestream supersonic Mach number. It is assumed to be a two-dimensional shock–turbulent boundary layer interaction problem. The Reynolds-averaged Navier–Stokes equations for an unsteady two-dimensional compressible flow without body forces or external heat addition can be written in conservation vector form for a Cartesian co-ordinate system as

$$\frac{\partial \mathbf{U}}{\partial t}+\frac{\partial \mathbf{E}}{\partial x}+\frac{\partial \mathbf{F}}{\partial y}=0. \tag{1}$$

The solution vector **U** and flux vectors **E** and **F** are given by

$$\mathbf{U}=\begin{vmatrix} \rho \\ \rho u \\ \rho v \\ \rho e \end{vmatrix}, \tag{2}$$

$$\mathbf{E}=\begin{vmatrix} \rho u \\ \rho u^2+p-\tau_{xx} \\ \rho uv-\tau_{xy} \\ (\rho e+p-\tau_{xx})u-\tau_{xy}v-q_x \end{vmatrix}, \tag{3}$$

$$\mathbf{F}=\begin{vmatrix} \rho v \\ \rho uv-\tau_{xy} \\ \rho v^2+p-\tau_{yy} \\ (\rho e+p-\tau_{yy})v-\tau_{xy}u-q_y \end{vmatrix}. \tag{4}$$

Here the viscous stress relations are

$$\tau_{xx}=\mu\left(\frac{4}{3}\frac{\partial u}{\partial x}-\frac{2}{3}\frac{\partial v}{\partial y}\right), \tag{5}$$

$$\tau_{xy}=\mu\left(\frac{\partial u}{\partial y}+\frac{\partial v}{\partial x}\right), \tag{6}$$

$$\tau_{yy}=\mu\left(\frac{4}{3}\frac{\partial v}{\partial y}-\frac{2}{3}\frac{\partial u}{\partial x}\right), \tag{7}$$

and the heat flux components are

$$q_x=k\frac{\partial T}{\partial x}, \tag{8}$$

$$q_y=k\frac{\partial T}{\partial y}. \tag{9}$$

The perfect gas law is

$$p=\rho(\gamma-1)e_1, \tag{10}$$

$$e=\left(e_1+\frac{u^2+v^2}{2}\right), \tag{11}$$

where ρ, p, e and e_1 denote the density, pressure, total energy and internal energy of the fluid, respectively, u and v are velocity components in the x- and y-direction, respectively, τ_{xx}, τ_{yy} and τ_{xy} are the stress components, and q_x and q_y are the heat fluxes. The viscosity, μ, is the sum of molecular and turbulent viscosities. The molecular viscosity is evaluated using Sutherland's formula.

ALGEBRAIC TURBULENCE MODEL

A two-layer equilibrium eddy viscosity model of Cebeci–Smith[8] is considered in the numerical simulation. In the inner region, the eddy viscosity is given by

$$\varepsilon_i=\rho\kappa^2y^2D^2\left|\frac{\partial u}{\partial y}\right|, \tag{12}$$

where κ is the von Karman constant (0·4) and D is the van Driest damping factor:

$$D=1-\exp\left[-y\frac{\left(\rho_w\mu_w\left|\frac{\partial u}{\partial y}\right|_w\right)^{1/2}}{26\,\mu_w}\right]. \tag{13}$$

The outer region is written as

$$\varepsilon_0=\frac{0{\cdot}0168\,u_e\delta^*}{\left[1+\left(\frac{y}{\delta}\right)^6\right]}, \tag{14}$$

where δ is the boundary layer thickness. δ^* is the kinematic displacement thickness, and is written

as

$$\delta^* = \int_0^\infty \left(1 - \frac{u}{u_e}\right) \mathrm{d}y. \tag{15}$$

The subscripts e, ∞, and w refer to the edge condition, freestream and wall values, respectively.

In modelling the strong disturbances, a relaxation modification is applied to the eddy viscosity obtained from the above equation as

$$\varepsilon_t = \varepsilon_{t0} + (\varepsilon_{teq} - \varepsilon_{t0})\left[1 - \exp\left(-\frac{x}{10\delta}\right)\right], \tag{16}$$

where ε_{t0} is the eddy viscosity at the origin of the disturbance. ε_{teq} is obtained from equations (12) and (14). Δx is the difference between the position of the disturbance and the position of the point of calculation. The above relation is adopted following Hankey and Shang.[9] An earlier measurement shows that the Reynolds stress attains exponentially a new equilibrium state.[10]

The eddy viscosity is given by

$$\varepsilon = \min\{\varepsilon_1, \varepsilon_0\}. \tag{17}$$

INITIAL AND BOUNDARY CONDITIONS

The initial flowfield and boundary conditions are shown schematically in Figure 1. The initial condition for the interior of the flowfield is a uniform flow. The flow variables at the top mesh boundary are set to either freestream values or values for a given shock strength so that the shock would impinge on the plate surface at the lower boundary at a given point. The post-shock conditions are calculated using the following relationships:[11]

$$\frac{\rho_p}{\rho_\infty} = \frac{(\gamma+1)M_\infty^2 \sin^2\theta}{(\gamma-1)M_\infty^2 \sin^2\theta + 2}, \tag{18a}$$

$$\frac{P_p}{P_\infty} = \frac{2\gamma M_\infty^2 \sin^2\theta - (\gamma-1)}{(\gamma+1)}, \tag{18b}$$

$$\frac{u_p}{u_\infty} = 1 - \frac{2(M_\infty^2 \sin^2\theta - 1)}{(\gamma+1)M_\infty^2}, \tag{18c}$$

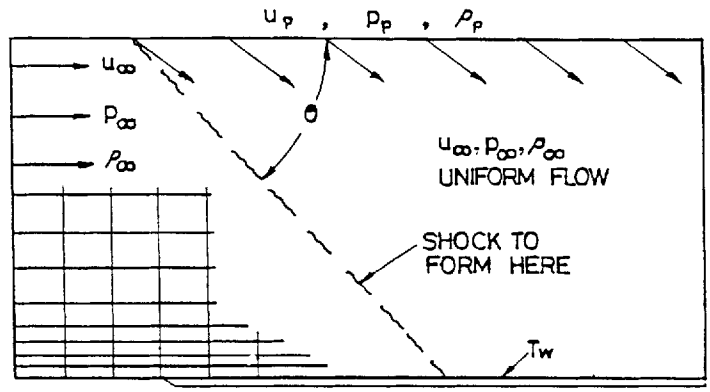

Figure 1. Initial flowfield for shock–boundary-layer interaction

$$\frac{v_p}{u_\infty}=\frac{2(M_\infty^2\sin^2\theta-1)}{(\gamma+1)M_\infty^2}\cot\theta, \tag{18d}$$

where γ is the ratio of the specific heats, subscripts p and ∞ represent the post-shock condition and the freestream condition, respectively, and θ is the oblique shock angle. At the solid wall boundary, no-slip conditions are implemented and the wall is assumed to be isothermal. For example, for no-slip and isothermal wall conditions, the expressions are

$$u_{i,1}=-u_{i,2}, \tag{19a}$$

$$v_{i,1}=-v_{i,2}, \tag{19b}$$

$$T_{i,1}=2T_w-T_{i,2}, \tag{19c}$$

where T_w is the wall temperature. A symmetric condition is used ahead of the leading of the plate as

$$\rho_y=u_y=v=T_y=0. \tag{19d}$$

The pressure is calculated at the centre of each cell. The present method uses a simple zeroth-order extrapolation procedure as

$$p_{i,1}=p_{i,2}. \tag{19e}$$

The pressure at the wall is taken to be equal to the pressure at the centre of the adjacent boundary cell, as given in equation (19e). Extensive numerical studies indicate that if the cell adjacent to the surface are small enough and the artificial dissipation terms are correctly treated, then the use of this weak condition for the pressure does not have a significant influence on the accuracy of the solution.

At the downstream boundary, the following extrapolation is used for the conservative variables:

$$U_{I,j}=3U_{I-1,j}-3U_{I-2,j}+U_{I-3,j}, \tag{19f}$$

where the subscript I represents the x-axis of the last node on the boundary. The flow leaving is either parabolic (near the plate) or hyperbolic (away from the plate) in the streamwise direction so that errors made here should not propagate in the upstream direction.

SOLUTION METHODOLOGY

The governing equations are solved by the explicit–implicit scheme developed by MacCormack.[12] The method consists of a predictor step and a corrector step, which can be written as follows. Predictor step:

explicit

$$\Delta U_{i,j}^n=-\Delta t\left[\left(\frac{E_{i+1,j}^n-E_{i,j}^n}{\Delta x}\right)+\left(\frac{F_{i,j+1}^n-F_{i,j}^n}{\Delta y}\right)\right], \tag{20a}$$

implicit

$$\left(I+\frac{\Delta t}{\Delta x}|A|_{i,j}^n\right)\delta U_{i,j}^*=\Delta U_{i,j}^n+\frac{\Delta t}{\Delta x}|A|_{i+1,j}^n\,\delta U_{i+1,j}^*, \tag{20b}$$

$$\left(I+\frac{\Delta t}{\Delta y}|B|_{i,j}^n\right)\delta U_{i,j}^{\overline{n+1}}=\delta U_{i,j}^*+\frac{\Delta t}{\Delta y}|B|_{i,j+1}^n\,\delta U_{i,j+1}^{\overline{n+1}}, \tag{20c}$$

update

$$U_{i,j}^{\overline{n+1}} = U_{i,j}^{n} + \delta U_{i,j}^{\overline{n+1}}. \tag{20d}$$

Corrector step:

explicit

$$\Delta U_{i,j}^{\overline{n+1}} = -\Delta t \left[\left(\frac{E_{i,j}^{\overline{n+1}} - E_{i-1,j}^{\overline{n+1}}}{\Delta x} \right) + \left(\frac{F_{i,j}^{\overline{n+1}} - F_{i,j-1}^{\overline{n+1}}}{\Delta y} \right) \right], \tag{20e}$$

implicit

$$\left(I + \frac{\Delta t}{\Delta x} |A|_{i,j}^{\overline{n+1}} \right) \delta U_{i,j}^{**} = \Delta U_{i,j}^{\overline{n+1}} + \frac{\Delta t}{\Delta x} |A|_{i-1,j}^{\overline{n+1}} \delta U_{i-1,j}^{**}, \tag{20f}$$

$$\left(I + \frac{\Delta t}{\Delta y} |B|_{i,j}^{\overline{n+1}} \right) \delta U_{i,j}^{n+1} = \delta U_{i,j}^{**} + \frac{\Delta t}{\Delta y} |B|_{i,j-1}^{\overline{n+1}} \delta U_{i,j-1}^{n+1}, \tag{20g}$$

update

$$U_{i,j}^{n+1} = \tfrac{1}{2}(U_{i,j}^{n} + U_{i,j}^{\overline{n+1}} + \delta U_{i,j}^{n+1}). \tag{20h}$$

Each step contains two stages. The first stage uses the explicit method, which is subject to restrictive explicit stability conditions. The second stage removes these stability conditions from the first stage into an implicit form. It is seen from the equations that the method requires the solution of the upper or lower bidiagonal matrix. Where I is a unit matrix, ∂U, δU^* and δU^{**} change in $\mathbf{U}$ with time step, $A = \partial \mathbf{E}/\partial \mathbf{U}$ and $B = \partial \mathbf{F}/\partial \mathbf{U}$ are the Jacobians of $\mathbf{E}$ and $\mathbf{F}$. The matrices $|A|$ and $|B|$ are the matrices with positive eigenvalues and are related to the Jacobians A and B. The overbars in the corrector sweeps indicate that the quantities are determined with update predictor values, the subscripts represent mesh point locations, and the superscripts represent the time, $t - n\Delta t$, Δt being the time step and n the time level. The scheme is of second-order accuracy in both time and space and captures the shock wave itself as the flowfield progresses from the initial condition to an asymptotic steady state.

ARTIFICIAL DISSIPATION

Shock embedded in the flowfield being solved computationally can often cause numerical oscillations and may lead to computer program failure due to physically unrealistic values of computing pressure. These oscillations may be caused by numerical truncation errors. The numerical oscillations can be reduced by refining the grids in the areas of shock locations. But the refinement of grids may be impractical where oscillations are of transient nature, caused by computationally startup or restart procedures. The grid refinement for each individual case is undesirable when the shock locations vary. A fourth-order pressure gradient damping concept is applied to increase the stability of the numerical algorithm. The fourth-order pressure damping terms are significant only in the area of high gradient, such as near shocks. The damping terms are introduced as a function of CFL number, so that its magnitude decreases as the time step is reduced. It is worth mentioning here that the CFL number is gradually reduced as the convergence is approached to avoid a possible steady-state solution dependence on the time increment, Δt.[13]

NUMERICAL RESULTS

The experiments selected for the present study were conducted by Johnson and Kaufman.[14] A summary of the test conditions is given below:

$$\theta_w = 10{\cdot}0^\circ,$$

$$M_\infty = 6{\cdot}0,$$
$$Re_\infty = 66{\cdot}1 \times 10^6 \text{ m}^{-1},$$
$$T_w/T_H = 0{\cdot}56,$$
$$x_s = 0{\cdot}3129 \text{ m},$$

where θ_w is the wedge angle of the shock generator, T_H is stagnation temperature and x_s is the shock-impinging distance measured from the leading edge. The computer used for the analysis was CDC CYBER 180/830 with 131k words memory available to the users. For turbulent flow, the high velocity gradients near the wall dictate an extremely fine mesh spacing in order to achieve adequate numerical resolution. The normal grid-point spacing is stretched exponentially to ensure adequate resolution of the flowfield, whereas a coarse constant grid size is used in the outer region. A grid independence check for the solution is performed using three different types of grid arrangement, such as 64×40, 72×32 and 82×42. Nearly identical solutions were obtained in all the cases. The data processing rate (CPU time per grid point, per time iteration) of $1{\cdot}922 \times 10^{-3}$ s was obtained for 82×42 grids.

A density contours plot is presented for shock–turbulent-boundary-layer interaction in Figure 2. A comparison is made between density contours and the Schlieren picture of Reference 14. The density contours pictures reproduce all the essential features of supersonic interacting flowfield as shown in the figure. From the contours plot, one can see the leading edge shock generated from the tip of the plate. The incident and reflected shock is also visible.

SPECTRAL ANALYSIS

Before we proceed with a detailed analysis of computer results, an initial comparison with available experimental data is made. The experimental results of Johnson and Kaufman[14] essentially provide the mean surface pressure and the mean heat transfer coefficient because they are obtained for specific experimental situations and locations. The measurements of surface

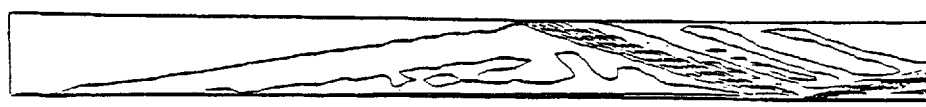

DENSITY CONTOURS

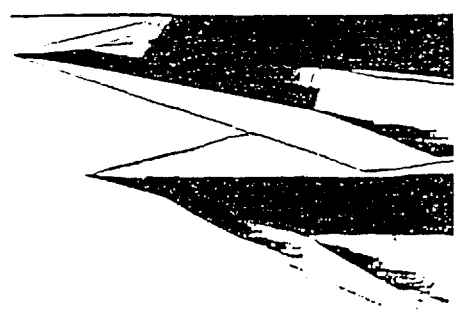

Figure 2. Density contours plot and Schlieren flow photograph

pressure and heat transfer coefficient distributions along the flat plate were computed using the following relations:

$$D_m = \frac{1}{\mathrm{TM}} \int_t^{t+\mathrm{TM}} D_m(t)\,\mathrm{d}t, \tag{21}$$

$$\langle D^2 \rangle_m = \left[\frac{1}{\mathrm{TM}} \int_t^{t+\mathrm{TM}} D_m^2(t)\,\mathrm{d}t - \left\{ \frac{1}{\mathrm{TM}} \int_t^{t+\mathrm{TM}} D_m(t)\,\mathrm{d}t \right\}^2 \right], \quad m = 1, 2, \tag{22}$$

where TM is the total period and is considered after 10 000 computation time steps. The subscript $m = 1$ is for surface pressure and $m = 2$ is for the heat transfer coefficient. Since the time increment for the pressure values is very small, the integral procedure were adopted using equations (21) and (22). The numerical results are shown in Figures 3–5 for the freestream Reynolds number $66{\cdot}1 \times 10^6\ \mathrm{m}^{-1}$. The skin friction distribution along the surface shows that the flow is separated. The experimental values of the mean pressure and the mean heat transfer coefficient are taken from Reference 14. The computed results compare well with the experimental data along the entire length of the flat plate.

Once the initial phase of computation was over, some periodicity in the flow characteristics was observed. The study of flowfield data was attempted in order to assess the separation zones, shock location and the amplitude and frequencies of sound pressure levels (SPL) and the heat flux.

As mentioned earlier, the flat plate was discretized by 82 equally spaced grids in the x-direction. At each grid point, during computation, a sufficient amount of time-dependent data was stored for frequency analysis. Owing to the limited computational resources available, the spectral analysis was carried out near the separation region for the freestream Reynolds number $66{\cdot}1 \times 10^6\ \mathrm{m}^{-1}$. In order to explore the sensitivity of unsteadiness, four sample stations near the separation zone are used, viz.

$$x = 0{\cdot}25425\ \mathrm{m},$$

$$x = 0{\cdot}29334\ \mathrm{m},$$

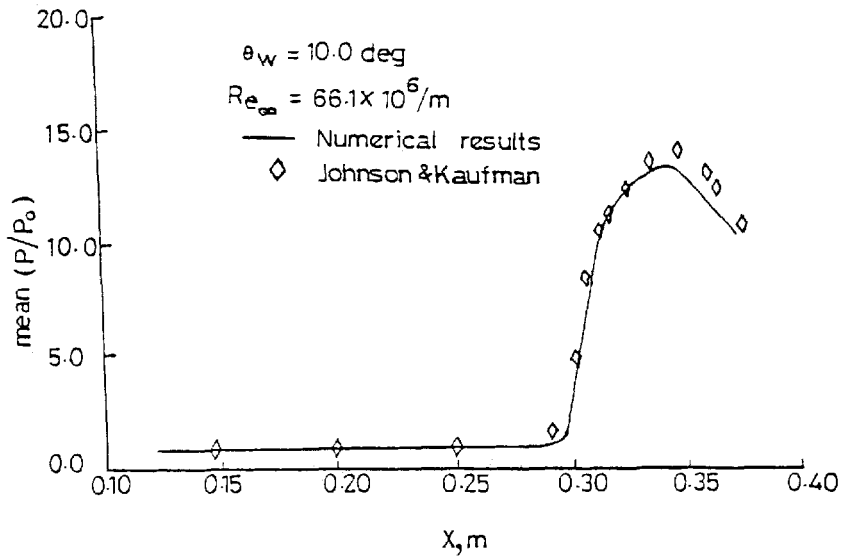

Figure 3. Comparison of interaction pressure ratio on a flat plate

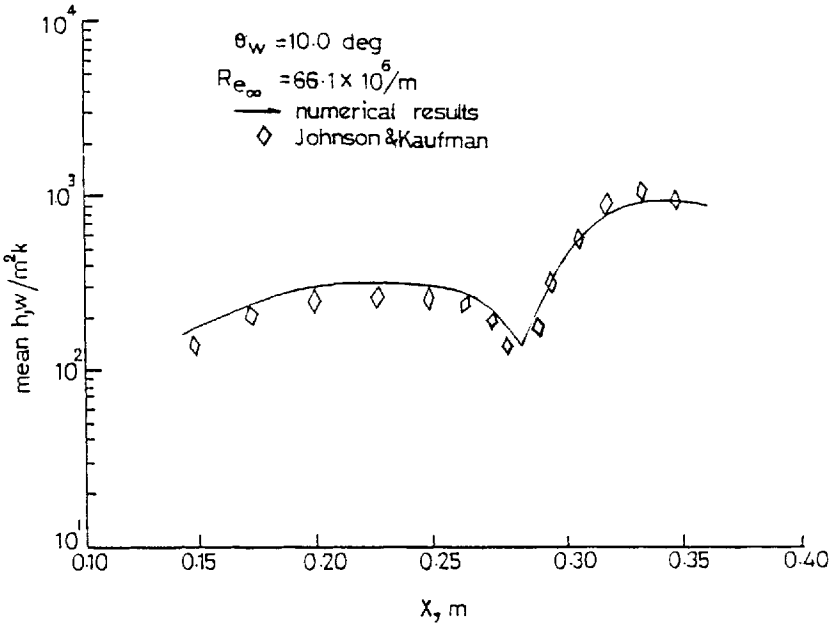

Figure 4. Heat transfer coefficient distribution on a flat plate

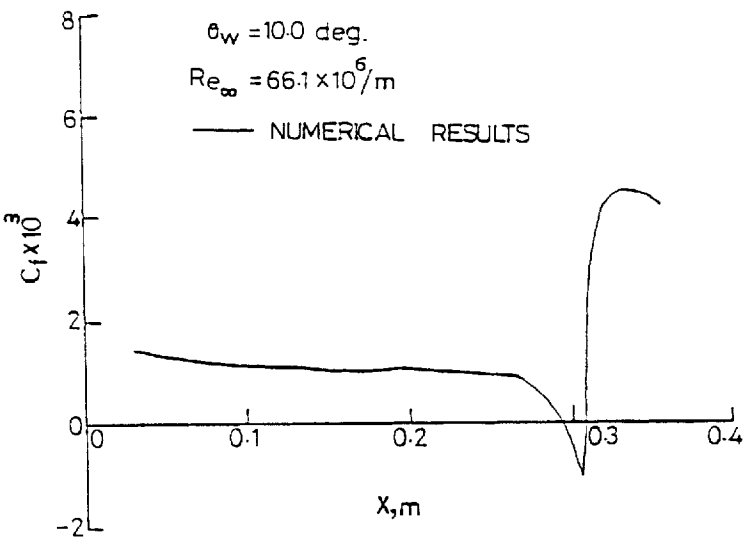

Figure 5. Skin friction variation along a flat plate

$$x = 0{\cdot}30450 \text{ m},$$

$$x = 0{\cdot}31009 \text{ m},$$

where x is measured from the leading edge of the flat plate. The surface pressure and the heat flux distribution at the aforementioned stations are shown in Figures 6 and 7 as a function of time.

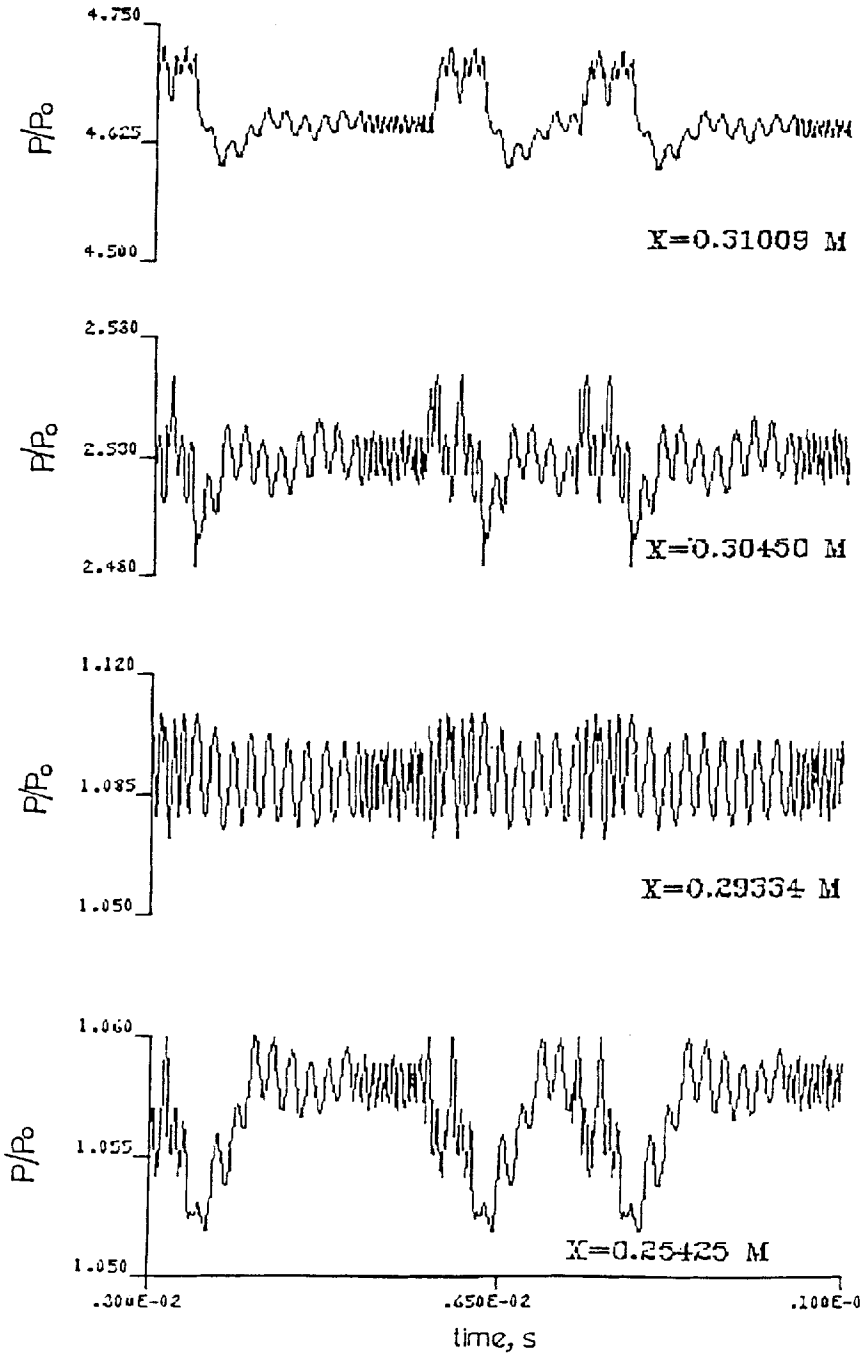

Figure 6. Pressure time history

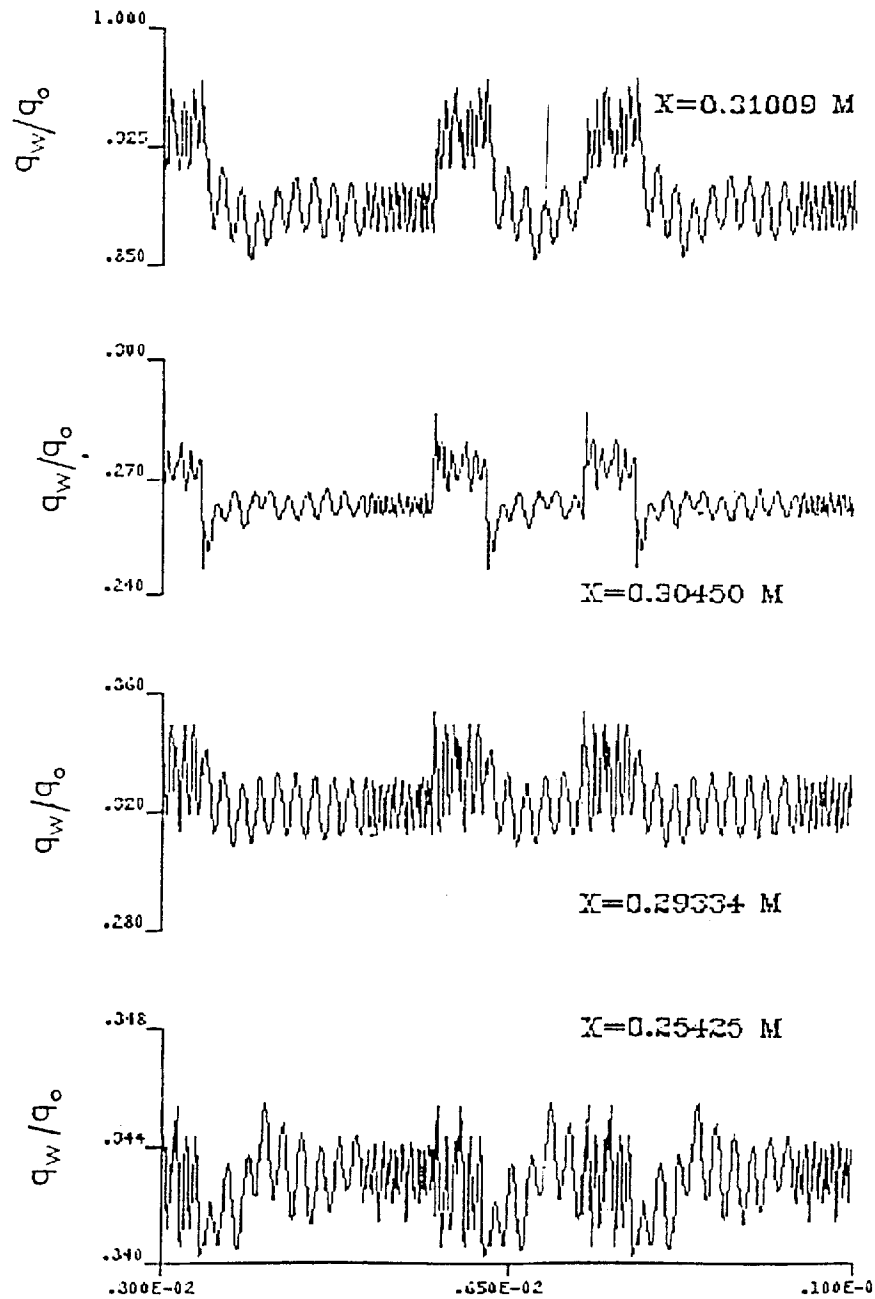

Figure 7. Heat flux time history

The scales are so chosen as to emphasize the amplitude variations. It can be observed from the pressure and the heat flux time history that periodicity in pressure and heat flux is manifest. Thus, the pressure and the heat flux data are free from the transitional phase, i.e. had the computation been continued for a very large time, the pressure and heat flux values would really be representative of the data.

An investigation of the unseparated flow[15] shows that the dominated frequency does not come into the picture in the calculation of pressure and heat flux quantities. This indicates a monotonic convergence of the numerical scheme.

The statistical approach of Purohit[16,17] shows that the last 3600 data points, starting after a sufficiently long time of computation, satisfy the criteria for the 'clean' data.

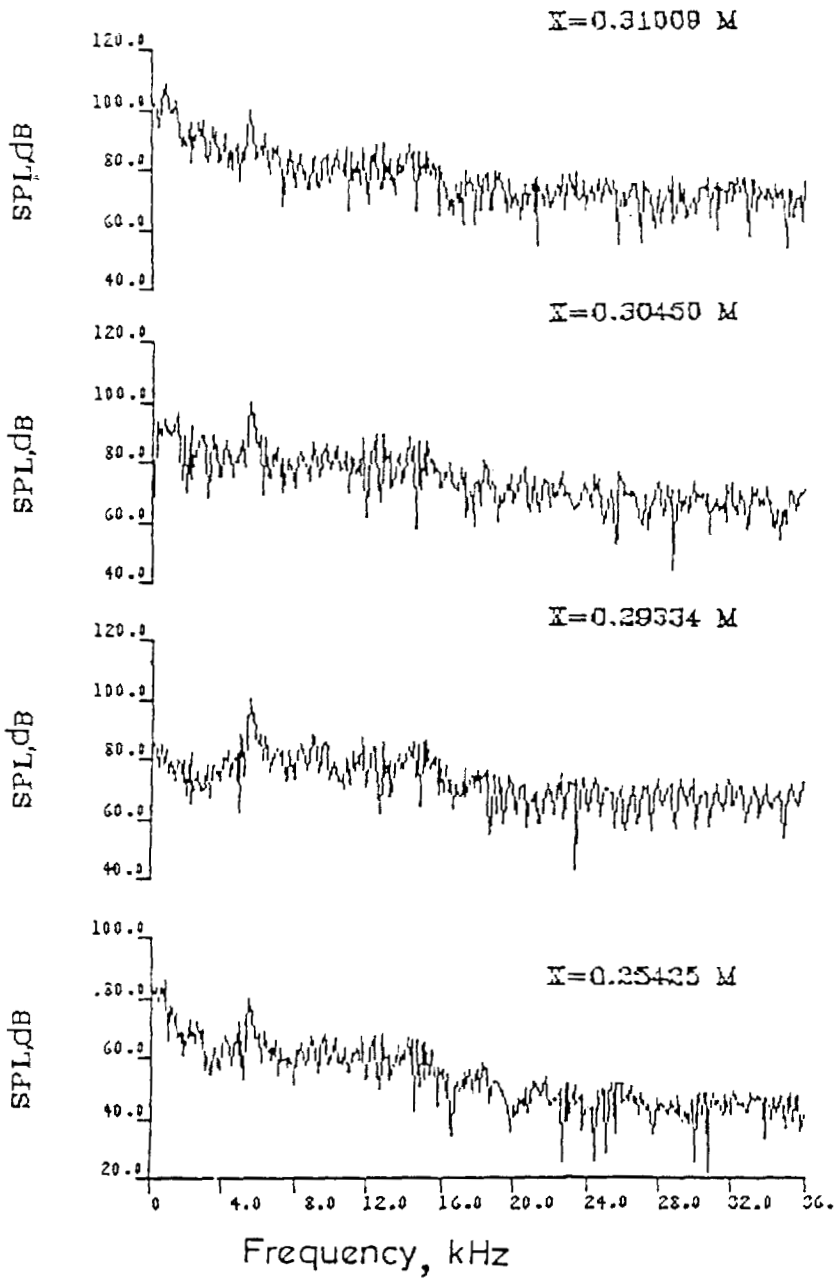

Figure 8. Spectral analysis of pressure fluctuations

A critical examination of the data points reveals that the secondary oscillations in the surface pressure and heat flux signatures, though bounded, cause only a slight increase as depicted in Figures 6 and 7. These oscillations may be due to the numerical procedure or due to the turbulence model. In practice, such fluctuations arise from the nature of the turbulence characteristics.[18]

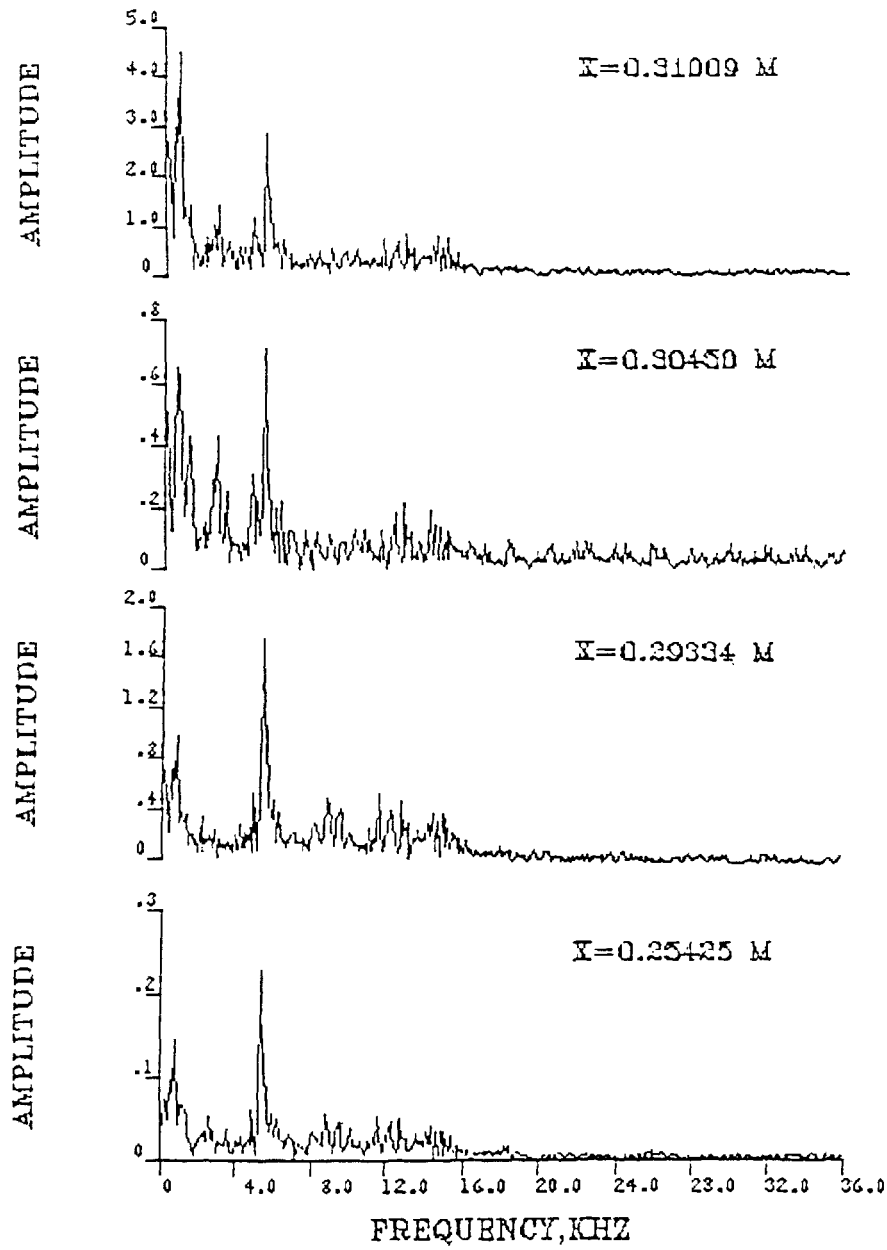

Figure 9. Spectral analysis of heat flux fluctuations

For the pressure and the heat flux data, a spectral analysis for all possible modes of oscillations was carried out using the fast Fourier transform subroutine (FFT) of the International Mathematical Statistical Library (IMSL). This subroutine converts the pressure histories from the time domain into the frequency domain. The pressure values have been converted from Pascals to decibels (dB) of sound pressure levels. The frequencies for which assessment was done were multiples of the fundamental frequency, 121 Hz. For pressure fluctuations, the sound pressure levels were computed in terms of the rms pressure referenced at 20 μN m^{-2}. Figures 8 and 9 show SPL and amplitude versus frequencies at different stations. The maximum sound pressure level of 110 dB occurs at about 845 Hz. Since no experimental results are available for this case, Hayashi *et al.*[7] have obtained a shock motion frequency of about 620 Hz at a freestream Mach number of 4·0, a Reynolds number, based on the shock-impinging distance, of $12{\cdot}7 \times 10^6$ and a wall-to-stagnation temperature ratio of 0·56. A comparison with these results revealed that the shock motion frequencies are increased with increased Mach number and Reynolds number. The wall pressure and the heat flux fluctuations show two peaks. From a comparison of the pressure and the heat flux fluctuations, we have found that the fluctuations in heat flux have qualitatively the same features as those in the wall pressure but have noticeable quantitative differences. Identical observations have been made in experiments by Hayashi *et al.*[7]

The spectral analysis of pressure and heat flux oscillations plots of Figures 8 and 9 shows two dominant frequencies, one at 845 Hz and another one at approximately 6 kHz. Considering the 845 Hz signal, this appears to be roughly in phase across the region examined, i.e. $x = 0{\cdot}25425$–$0{\cdot}31009$ m. The sound pressure level of the pressure fluctuations also increases as the distance, x, increases. This is consistent with 'a solid body motion' of the interaction region since the local amplitude would be a function of the slope of the pressure curve, as depicted in Figure 3. However, the heat fluxes plots in Figure 9 also apparently phase, both with each other and with the pressure. This behaviour is also evident from the pressure–time plots of Figure 6 as well as from the heat flux history of Figure 7. Prior to the separation point, the slope of the heat transfer curve is negative, as can be seen in Figure 4. The heat flux should, therefore, be in antiphase with the pressure in this region. But the numerical analysis shows both in the same phase. It is difficult to explain this inconsistency. Beyond this point, the slope is positive and the pressure and the heat flux fluctuations are in phase. The present analysis has modelled a physical mechanism of unsteadiness at the reattachment point of shock-separated supersonic flows.

CONCLUSIONS

The shock–turbulent-boundary-layer interaction was analysed using a finite difference method in conjunction with the eddy viscosity relaxation term. The following conclusions are made, based on this investigation:

1. Flow separation was noticed at a freestream Mach number of 6, a freestream Reynolds number of $66{\cdot}1 \times 10^6$ m^{-1} and a wall-to-stagnation temperature ratio of 0·56.
2. The fluctuations in the wall heat flux have quantitatively the same features as those of the wall pressure, but are different quantitatively.
3. A spectral analysis for all possible modes of oscillations was carried out using fast Fourier transform. The maximum shock motion frequency is about 845 Hz. The maximum sound pressure levels was 110 dB near the separation point.

REFERENCES

1. A. L. Kistler, 'Fluctuating wall pressure under a separated supersonic flow', *J. Acoustic Soc. Am.*, **36**, 543–550 (1964).
2. D. S. Dolling and M. T. Murphy, 'Unsteadiness of the separation shock wave structure in a supersonic compression ramp flowfield', *AIAA J.*, **21**, 1628–1633 (1983).

3. T. T. Tan, 'An experimental investigation of unsteadiness in swept shock wave/turbulent boundary layer interactions', *Ph.D. Dissertation*, Mechanical and Aerospace Engineering Department, Princeton University, Princeton, NJ, 1986.
4. M. Hayashi, S. Aso and A. Tan, 'Fluctuations of wall pressure in interacting region of oblique shock wave and turbulent boundary layer', *Technology Reports of the Kyushu University*, Vol. 59, No. 1, 1986, pp. 75–82.
5. C. F. Coe, W. J. Chyu and J. B. Dods, Jr. 'Pressure fluctuations underlying attached and supersonic turbulent boundary layers and shock waves', in H. T. Nagaamatsu (ed.), *Progress in Astronautics and Aeronautics Series*, Vol. 38, AIAA, Washington, 1975, pp. 243–262.
6. D. S. Dolling and J. P. Dussauge, 'Fluctuating wall pressure measurements, A survey of measurements and measuring techniques in rapidly distorted compressible turbulent boundary layers', *AGRDograph*, 315, Chap. 2, 1988.
7. M. Hayashi, S. Aso and A. Tan, 'Fluctuation of heat transfer in shock wave/turbulent boundary layer interaction', *AIAA J.*, **27**(4), 339–404 (1989).
8. T. Cebeci and A. M. O. Smith, *Analysis of Turbulent Boundary Layers*, Academic Press, NY, 1974.
9. W. L. Hankey and J. S. Shang, 'An analysis of pressure oscillation in an open cavity', *AIAA J.*, **18**, 892–898 (1980).
10. R. Narasimha and A. Prabhu, 'Equilibrium and relaxation in turbulent wakes', *J. Fluid Mech.*, **54**, 1–17 (1972).
11. Ames Research Staff, 'Equations, tables and charts for compressible flow', *NACA Report 1135*, 1953.
12. R. W. MacCormack, 'A numerical method for solving the equations of compressible viscous flow', *AIAA J.*, **20**, 1275–1281 (1982).
13. R. N. Gupta, P. A. Gnoffo and R. W. MacCormack, 'A viscous shock-layer flowfield analysis by an explicit–implicit method', *NASA TM 84668*, 1983.
14. C. B. Johnson and L. G. Kaufman II, 'Interference heating from interaction of shocks with turbulent boundary layers at Mach 6', *NASA TN-D 7649*, 1974.
15. R. C. Mehta, 'Numerical solution of shock wave/turbulent boundary layer interaction', *Ph.D. Thesis*, Indian Institute of Technology, Madras, 1992.
16. S. C. Purohit, 'A Navier–Stokes solution for bulbous shroud', *J. Spacecraft Rockets*, **23**(6), 590–596 (1986).
17. S. C. Purohit, 'Supersonic flow simulation for boattail heatshield', *Aeronaut. J.*, **91**(904), 183–189 (1987).
18. S. C. Purohit, J. S. Shang and W. L. Hankey, 'Numerical simulation of flow around a three-dimensional turret', *AIAA J.*, **21**, 15533–15540 (1983).